

Electronic Supplementary Information (ESI†) for

# **MoS<sub>2</sub>-Capped Cu<sub>x</sub>S Nanocrystals: A New Heterostructured Geometry of Transition Metal Dichalcogenides for Broadband Optoelectronics**

*Yuan Li,<sup>a,b</sup> Akshay A. Murthy,<sup>a</sup> Jennifer G. DiStefano,<sup>a</sup> Hee Joon Jung,<sup>a,b</sup> Shiqiang Hao,<sup>a</sup> Cesar J. Villa,<sup>a</sup> Chris Wolverton,<sup>a</sup> Xinqi Chen,<sup>b,c,\*</sup> Vinayak P. Dravid<sup>a,b,d,\*</sup>*

<sup>a</sup> Department of Materials Science and Engineering, <sup>b</sup> Northwestern University Atomic and Nanoscale Characterization Experimental (NUANCE) Center, <sup>c</sup> Department of Mechanical Engineering, and <sup>d</sup> International Institute for Nanotechnology (IIN), Northwestern University, Evanston, Illinois 60208, USA

\*Corresponding author

Xinqi Chen: [x-chen@northwestern.edu](mailto:x-chen@northwestern.edu)

Vinayak P. Dravid: [v-dravid@northwestern.edu](mailto:v-dravid@northwestern.edu)

## S1. Experimental details

### S1.1. Materials and methods

Molybdenum trioxide (99.9995%) and sulfur powders (99.9995%) were purchased from Alfa Aesar (Ward Hill, MA). High-temperature annealing, sulfurization and chemical vapor deposition was conducted in a Lindberg Blue M tube furnace. Copper evaporation was conducted on the Lesker Nano38 (Kurt J. Lesker Company). The FEI Quanta ESEM was used for the electron-beam lithographic fabrication of field-effect transistor devices. Electronic measurements were conducted using a Signatone S-1160 Probe Station. Raman spectra and photoluminescence spectra were collected on the Horiba LabRAM HR Evolution Confocal Raman System. A laser power of  $\sim 1 \mu\text{W}$  was used to avoid the possible influence of optical heating to the Raman scattering and photoluminescence emission. X-ray photoelectron spectroscopy (XPS, Thermo Scientific ESCALAB 250Xi) was used for binding energy analysis. Hitachi SU8030 SEM and JEOL ARM300F GrandARM S/TEM were used for morphological and structural characterizations.

### S1.2. Chemical vapor deposition of $\text{Cu}_x\text{S}@ \text{MoS}_2$

The Si/SiO<sub>2</sub> substrates were cleaned with the piranha solution (4:1 H<sub>2</sub>SO<sub>4</sub>:H<sub>2</sub>O<sub>2</sub>) at 110 °C for 30 min before use. A Cu film of 4 nm was deposited on the Si/SiO<sub>2</sub> substrate, followed by a high-temperature annealing at 600 °C for 15 min in N<sub>2</sub> environment to obtain well-dispersed Cu nanoparticles. The sample was sulfurized by reacting with sulfur vapor at 600 °C for 30 min. The following MoS<sub>2</sub> growth was conducted *via* a chemical vapor deposition process. Briefly, the substrate was put face down on an alumina boat containing 10 mg MoO<sub>3</sub>. Another boat containing 120 mg sulfur powders was put in the upstream side. N<sub>2</sub> gas with a flow rate of 200 sccm was used as the carrier gas. The furnace was first heated up to 300 °C and kept for 30 min, and then ramped

to the growth temperature (650 °C). The growth was continued for 5 min with a N<sub>2</sub> flow rate of 20 sccm. The furnace was then slowly cooled down to ambient temperature.

### S1.3. Fabrication of field-effect transistor

The device fabrication was conducted using a standard electron-beam lithography process. Briefly, PMMA (950 A3) was spin-coated on the substrate with a spin rate of 4000 rpm for 45 s. The substrate was soft-baked at 180 °C for 3 min. The pre-designed contact mask was aligned to the device target region. The substrate was then exposed by an electron-beam with area dose of 400-600 μC/cm<sup>2</sup>. After developing, a 5-nm Cr film and 50-nm Au film were evaporated onto the substrate to serve as the contact. The sample was then lifted off in hot acetone and finally annealed at 250 °C for 2 h (in N<sub>2</sub> environment) before electric characterizations. The electric test was conducted using a standard Signatone four-probe electric station at ambient temperature.

### S1.4. Discrete Dipole Approximation (DDA) modeling

The computation of absorbance and surface electric field distribution of isolated targets (Cu<sub>x</sub>S, Cu<sub>x</sub>S@MoS<sub>2</sub>) were performed using the Discrete Dipole Approximation algorithm implemented in the DDSCAT 7.2 code developed by Draine and Flatau.<sup>1</sup> The Cu<sub>x</sub>S was modeled as a 50 × 25 × 25 nm<sup>3</sup> rectangular target, while the Cu<sub>x</sub>S@MoS<sub>2</sub> was built up using the same Cu<sub>x</sub>S target capped with 6-layer MoS<sub>2</sub> (Figure 1b). These targets were built as a lattice of polarizable cubic elements or dipoles with position  $r_i$  and possibility  $\alpha_i$  ( $i = 1, 2, \dots, N$ ). In the simulation, the targets were excited by a monochromatic incident wave vertical to the cross-section of the heterostructures, and the induced extinction and absorption of the targets were calculated by

$$C_{abs} = \frac{4\pi k}{|E_0|^2} \sum_{i=1}^N \{Im[P_i(\alpha_i^{-1})^* P_i^*] - \frac{2k^3}{3} |P_i|^2\} \quad (1)$$

here \* represents complex conjugate,  $k = \frac{2\pi}{\lambda}$  is the wave number of the incident wave and  $E_0$  is its amplitude,  $E_{loc,i}$  is the local field calculated from the sum of the incident radiation field of dipole  $i$  and the field radiated by the other  $N-1$  dipoles, and  $P_i$  is the polarization induced in dipole  $i$ , expressed as

$$P_i = \alpha_i E_{loc,i}(r_i). \quad (2)$$

The absorption efficiency ( $Q_{abs}$ ) of the simulated targets (Figure 5A) were calculated from

$$Q_{abs} = C_{abs}/(\pi a_{eff}^2) \quad (3)$$

where  $a_{eff}$  is the effective radius of a sphere with volume  $(\frac{4\pi a_{eff}^3}{3})$  equal to the volume of the heterostructured targets.

As mentioned, the strong light-matter interaction at the visible region leads to the generation of SPR, which further forms a constant localized electric field on/near the surface of the targets.<sup>2</sup> The intensity of electric field was theoretically calculated from the sum of the incident radiation field of dipole  $i$  and the field radiated by the other  $N-1$  dipoles, as shown in the following equation,

$$E_{loc,i}(r_i) = E_{inc,i} + E_{dip,i} = E_0 \exp(ikr_i) - \sum_{j \neq i} A_{ij} P_j. \quad (4)$$

The interaction matrix A can be represented as

$$A_{ij} P_j = \frac{\exp(ik|r_{ij}|)}{|r_{ij}|^3} \left\{ k^2 r_{ij} \times (r_{ij} \times P_j) + \frac{1-ik|r_{ij}|}{|r_{ij}|^2} \times \left[ |r_{ij}|^2 P_i - 3r_{ij}(r_{ij} P_j) \right] \right\}$$

$$j = 1, 2, \dots, N, j \neq i \quad (5)$$

where  $|r_{ij}| = |r_i - r_j|$  and  $P$  is the polarization vector.

### S1.5. Density functional theory calculation

Density functional theory (DFT) electronic structure calculations were performed in order to gain insights into the various band alignments in these materials. The calculations were performed using the generalized gradient approximation with PBE<sup>3</sup> functional for the exchange correlation functional and projector augmented wave potentials as implemented in VASP (Vienna Ab-initio Simulation Package).<sup>4</sup> All structures are fully relaxed with respect to cell vectors and cell-internal positions. The electronic DOS (density of states) is calculated from the relaxed structures using the tetrahedron method with Blöchl corrections.

For the band structure and work function calculations of  $\text{Cu}_{1.8}\text{S}$  and  $\text{Cu}_{1.9}\text{S}$ , we consider the difference Cu vacancies to get corresponding compositions. In other words, starting from a primitive  $\text{Cu}_2\text{S}$  cell containing  $\text{Cu}_8\text{S}_4$  atoms, we calculate  $\text{Cu}_7\text{S}_4$  as  $\text{Cu}_{1.8}\text{S}$  and  $\text{Cu}_{15}\text{S}_8$  as  $\text{Cu}_{1.9}\text{S}$ . To approve the relative band alignments of  $\text{MoS}_2$  systems, we also utilize the findings of Van de Walle and Neugebauer, who demonstrated a universal alignment of the electronic transition level of hydrogen in a wide range of materials including semiconductors, insulators and even aqueous solutions.<sup>5</sup> Hence, to infer the band alignment, we compute the energies of H defects in the rock salt compounds of interest, assume alignment between these H energies, and then extract the band alignment of the compounds. To align the valance band maximum position of each system, we consider the defect formation energies of various charge states of interstitial  $Hq$  ( $q = -1, 0, 1$ ) by placing H in the host material, calculating the total energy of this structure, and subtracting the energy of the corresponding pure host material, hydrogen chemical potential, and electron chemical potential:<sup>5</sup>

$$E_f(Hq) = E_{tot}(Hq) - E_{tot}(bulk) - 0.5E_{tot}(H_2) + q(E_V + \Delta E + E_F), \quad (6)$$

where  $E_V$  and  $E_F$  are valence band maximum and Fermi level (relative to the VBM). To select the most favorable interstitial H binding sites in host materials, multiple binding configurations are calculated. The electrostatic potential correction term  $\Delta E$  is calculated by inspecting the potential in the supercell far from the impurity and aligning it with the electrostatic potential in bulk.<sup>6</sup>

## References

1. Draine, B. T., Flatau, P. J. User guide for the discrete dipole approximation code DDSCAT 7.3. *arXiv preprint arXiv:1305.6497*, **2013**.
2. Wu, J.; Shi, W.; Chopra, N. Optical properties of gold/multilayer-graphene/carbon nanotube hybrid materials. *Carbon* **2014**, *68*, 708.
3. Perdew, J. P.; Burke, K.; Ernzerhof, M. Generalized Gradient Approximation Made Simple. *Phys. Rev. Lett.* **1996**, *77*, 3865.
4. Kresse, G.; Furthmüller, Efficient iterative schemes for ab initio total-energy calculations using a plane-wave basis set. *J. Phys. Rev. B* **1996**, *54*, 11169.
5. Van de Walle, C. G.; Neugebauer, J. Universal alignment of hydrogen levels in semiconductors, insulators and solutions. *Nature* **2003**, *423*, 626.
6. Van de Walle, C. G.; Neugebauer, J. First-principles calculations for defects and impurities: Applications to III-nitrides. *J. Appl. Phys.* **2004**, *95*,385.

## S2. Supplementary figures

**Fig. S1.** XRD pattern of  $\text{Cu}_x\text{S}@/\text{MoS}_2$  heterostructures and XRD JCPDS cards analysis.

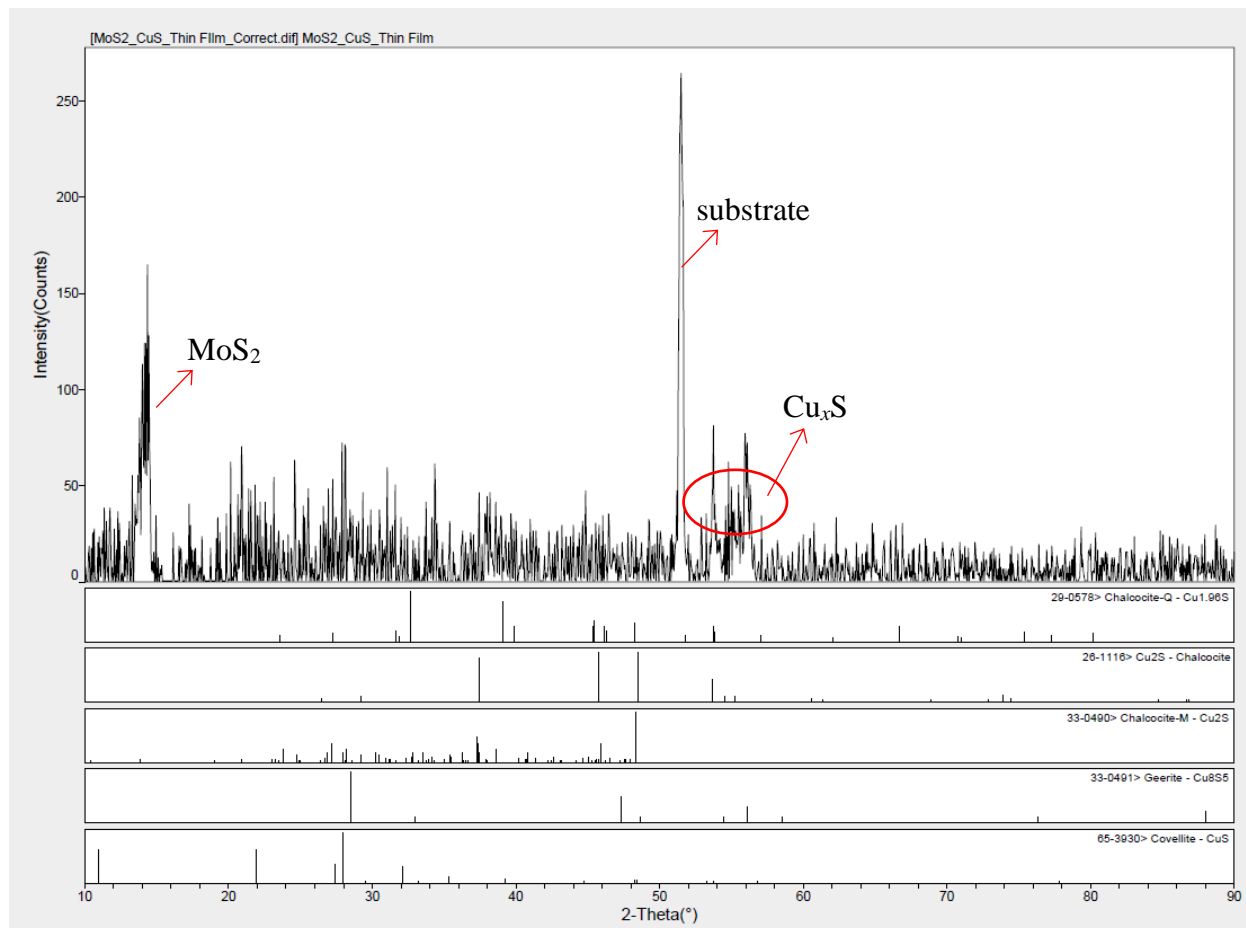


**Fig. S2. Preparation of control sample,  $\text{Cu}_x\text{S}/\text{MoS}_2$ .** (a) Schematic illustrating the transfer steps of conventional CVD-grown  $\text{MoS}_2$  monolayer onto the  $\text{Cu}_x\text{S}$  nanocrystals. (b) Optical image and (c) SEM image of the resultant  $\text{Cu}_x\text{S}/\text{MoS}_2$ . The arrows in (c) indicate various twisted morphology of  $\text{MoS}_2$  film due to the presence of underlying  $\text{Cu}_x\text{S}$  nanocrystals.

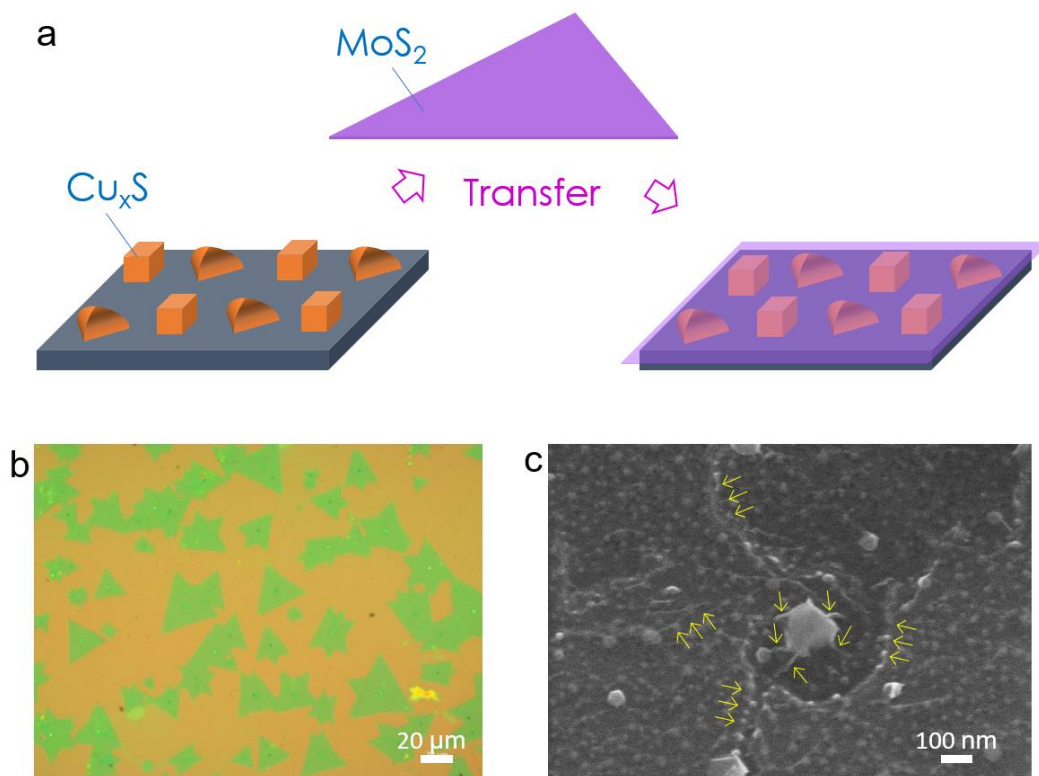


**Figure S3. DFT-calculated band structures.** (a)  $\text{Cu}_2\text{S}$ , (b)  $\text{Cu}_{1.9}\text{S}$ , and (c)  $\text{Cu}_{1.8}\text{S}$ . Note: The work function of  $\text{Cu}_2\text{S}$ ,  $\text{Cu}_{1.9}\text{S}$ , and  $\text{Cu}_{1.8}\text{S}$  is 4.78 eV, 4.81 eV, and 4.85 eV, respectively.

